Perovskite-Type LaSrMnO Electrocatalyst with Uniform Porous Structure for an Efficient Li–O₂ Battery Cathode

Yanbing Yang,[†] Wei Yin,[§] Shiting Wu,[‡] Xiangdong Yang,[†] Wei Xia,[‡] Yue Shen,[§] Yunhui Huang,[§] Anyuan Cao,*[,‡] and Quan Yuan*[,†]

[†]Key Laboratory of Analytical Chemistry for Biology and Medicine (Ministry of Education), College of Chemistry and Molecular Sciences, Wuhan University, Wuhan 430072, China

[‡]Department of Materials Science and Engineering, College of Engineering, Peking University, Beijing 100871, China

[§]State Key Laboratory of Material Processing and Die&Mold Technology, School of Materials Science and Engineering, Huazhong University of Science and Technology, Wuhan, Hubei 430074, China

Ⓢ *Supporting Information*

ABSTRACT: Perovskite is an excellent candidate as low cost catalyst for Li–O₂ cells. However, the limited porosity, which impedes molecular transport, and the inherent low electronic conductivity are the main barriers toward production of high-performance electrodes. Here, we designed a hierarchical porous flexible architecture by coating thin mesoporous yet crystalline LaSrMnO layers throughout a graphene foam to form graphene/*meso*-LaSrMnO sandwich-like nanosheets. In this well-designed system, the macropore between nanosheets facilitates O₂ and Li⁺ diffusion, the mesopore provides large surface area for electrolyte immersion and discharge products deposition, the perovskite phase catalyst decreases reactive overpotential, and the graphene serves as conductive network for electrons transport. When used as a freestanding electrode of Li–O₂ cell, it shows high specific capacity, superior rate capability, and cyclic stability. Combination of mesoporous perovskites with conductive graphene networks represents an effective strategy for developing efficient electrodes in various energy storage systems.

KEYWORDS: perovskite, mesoporous, LaSrMnO, graphene, LiO₂ cell
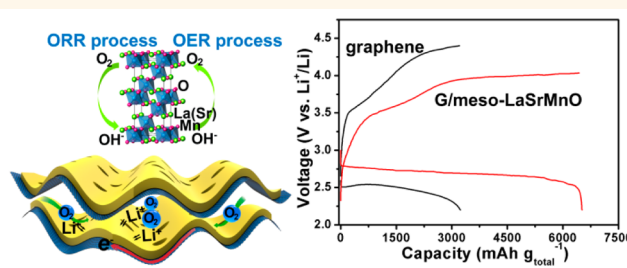
Perovskite-based ABO₃ composite oxides with great structural/chemical flexibility represent an important class of multifunctional materials and are considered to be promising candidates as high-performance catalysts in CO oxidation,[1] CH₄ combustion,[2] and NOₓ and SO₂ reduction.[3] The unique defective structure and disorder-free channels of oxygen vacancies offer a large number of active sites in catalytic reactions.[4–7] The catalytic property of perovskite is particularly useful in developing next-generation high energy storage devices such as Li–O₂ cells with high energy density and low cost.[8–12] Typically, an ideal Li–O₂ cell electrode should possess several key features including a uniform porous structure for O₂ and Li⁺ diffusion and large surface area for discharge product deposition,[13,14] a conductive pathway for electrons transport,[15,16] and efficient catalyst to reduce overpotential as well as avoid polarization.[17,18] A critical element in the pursuit of a high-performance Li–O₂ cell with large capacity and long cycling life is the cathode catalyst. To this end, perovskite materials have tunable physical and chemical properties and can catalyze both oxygen reduction reaction (ORR) and oxygen evolution reaction

(OER),[19,20] making them a promising low-cost candidate to serve as cathode catalyst compared with noble metal.[21–23] It has been reported that transition-metal oxide perovskite with an e_g filling (σ*-orbital occupation) of ~1 has maximum catalytic activity, and the LaMnO₃₊σ deserves particular attention because of the improved B-site transition-metal–oxygen covalency between the metal 3d and oxygen 2p orbitals.[4] Creating mesopores within La₀.₈Sr₀.₂MnO₃ (LaSrMnO) can increase the active surface area and enhance molecular transport. Thus far, down-sized LaSrMnO nanoparticles or porous nanotubes composed of aggregated nanoparticles have been made by sol–gel or electrospinning methods, and their applications as Li–O₂ cell cathodes have been exploited.[5,24–26] However, since mesopores only exist between the aggregated nanoparticles, those LaSrMnO structures suffered from low porosity and small

Scheme 1. (a) Illustration of the Fabrication Process of G/*meso*-LaSrMnO Foams, Including Macroscopic Model of the original G Foam Dipped into the Precursor Solution and the Resulting Porous Framework Composed of G/*meso*-LaSrMnO Nanosheets[a] (b) Photos and Structural Models of G/*meso*-LaSrMnO Foam under Different Deformations
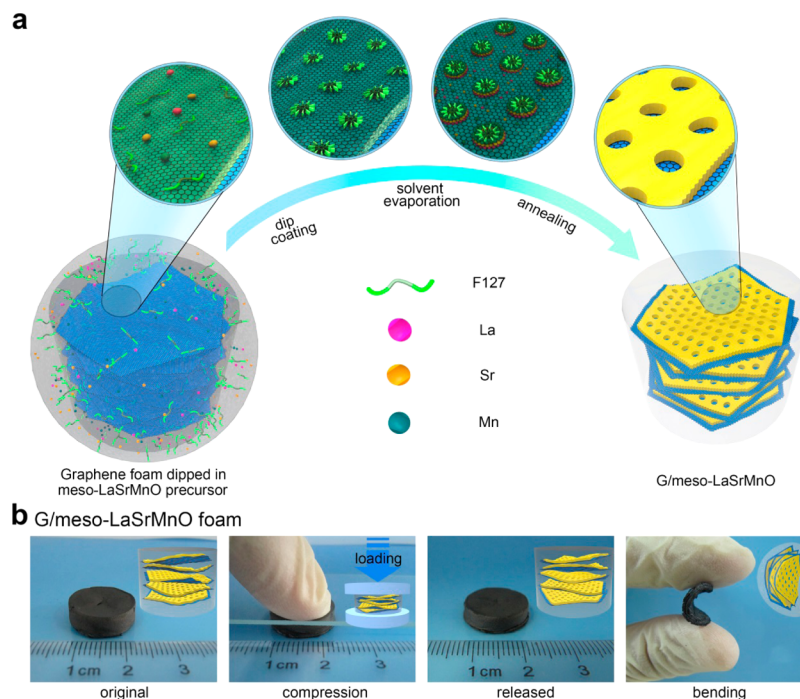

[a]The precursor solution and surfactant undergo self-assembly during an EISA process and form a *meso*-LaSrMnO layer supported on graphene nanosheets by annealing.

surface area, which results in limited Li$^+$ and O$_2$ transport channels and further leads to reduced discharge capacity. In addition, the inherent low electrical conductivity of LaSrMnO needs to be overcome for production of high-performance electrodes. In addition, polymer binders used in LaSrMnO powders may disturb the interconnected perovskite network as well as decrease the effective surface area and electrode conductivity. To date, controlled synthesis of mesoporous yet crystalline LaSrMnO materials with uniform pore distribution remains a great challenge.

Herein, to address the key challenges in the synthesis of well-defined and uniform mesoporous LaSrMnO (*meso*-LaSrMnO) nanosheets, we demonstrate, for the first time, a novel approach of preparing hierarchical architectures by coating thin *meso*-LaSrMnO layers throughout a graphene foam (G-foam) to form graphene/*meso*-LaSrMnO (G/*meso*-LaSrMnO) sandwich-like nanosheets. Owing to its unique characteristics including superior electrical conductivity, high surface area, and excellent mechanical flexibility, graphene can serve as a porous flexible template and conductive network for constructing macroscopic three-dimensional (3D) electrodes.[27−30] Combination of graphene with *meso*-LaSrMnO to form hierarchical composite structures has not been explored before. In order to obtain *meso*-LaSrMnO with uniform pore size and crystalline framework walls throughout the G-foam, we adopt a dip-coating and evaporation induced self-assembly (EISA) process. This involves the formation of uniform micelles of surfactant template and simultaneous hydrolysis and condensation of precursors in the self-assembly process, which is used in the synthesis of mesoporous materials.[31,32] In this well-designed system, the 3D hierarchical porous structure is an optimized configuration for facilitating O$_2$ transport, electrolyte immersion, Li$^+$ diffusion

and collection of the solid-state discharge products when used as a freestanding Li−O$_2$ cell electrode. It is anticipated that our demonstration of flexible perovskite electrode not only represents a method for fabricating high performance energy storage devices but also for constructing multifunctional configurations in cost-effective and time saving ways.

Scheme 1a illustrates our design principle and synthetic route toward uniform *meso*-LaSrMnO nanosheets supported on graphene. First, the graphene oxide sheets are prepared from graphite by a modified Hummers method,[35] and then a subsequent hydrothermal treatment at 75 °C with the assistance of ascorbic acid results in the formation of porous G-foam (see the Experimental Section). Second, a dip-coating method is adopted by immersing the G-foam into a precursor solution composed of La(NO$_3$)$_3$, Sr(NO$_3$)$_2$, Mn(NO$_3$)$_2$, and surfactant F127. The foam is further removed from the precursor solution and subjected to the EISA process at 60 °C. As the solvent evaporation proceeds, the concentration of the F127 block copolymers increases and eventually arranges into uniformly dispersed micelles. At the same time, the precursors interact with the hydrophilic part of surfactants, resulting in coassembly of precursors around the surfactant micelles and form a continuous mesophase. The controlled slow hydrolysis and condensation of the precursors by the coordination agent of concentrated HNO$_3$ and citric acid favors heterogeneous nucleation of LaSrMnO on graphene sheets rather than self-nucleating into separate nanoparticles. After subsequent heat treatments at 100 °C (for removal of residue water and ethanol) and 140 °C (for valence state change of Mn element), respectively, and a final annealing at 650 °C under inert atmosphere, gives a hierarchical 3D porous structure composed of mesopores in LaSrMnO and macropore between G/*meso*-LaSrMnO nanosheets. It is worth mentioning
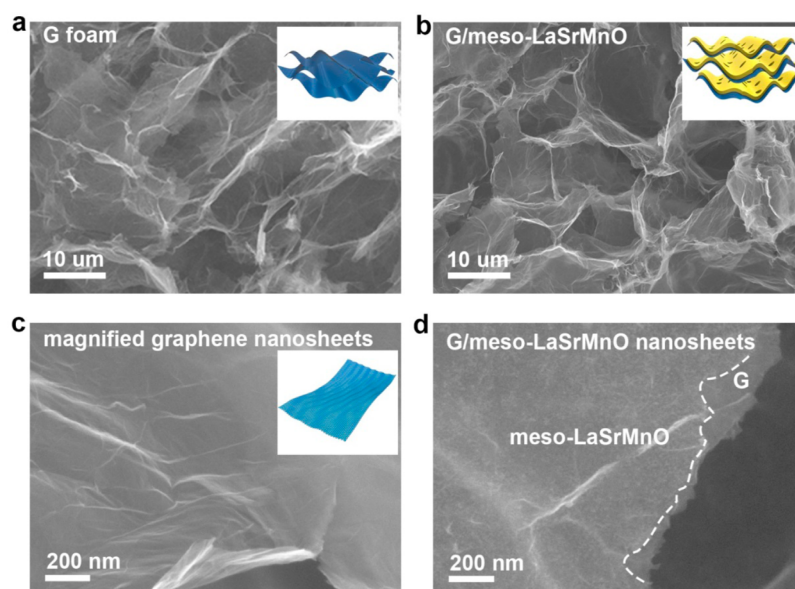
Figure 1. Structural characterization of G-foam and G/*meso*-LaSrMnO composite. SEM images of (a) original G foam, (b) hybrid G/*meso*-LaSrMnO foam. Insets of (a, b) are structural models of porous G and G/*meso*-LaSrMnO. The G/*meso*-LaSrMnO retains original porous morphology compared with G-foam. High-resolution SEM images of (c) G-foam and (d) G/*meso*-LaSrMnO. The rough surface of G/*meso*-LaSrMnO and interface between G and *meso*-LaSrMnO indicates the successful coating. Inset of (c) is the structural model of graphene nanosheets.
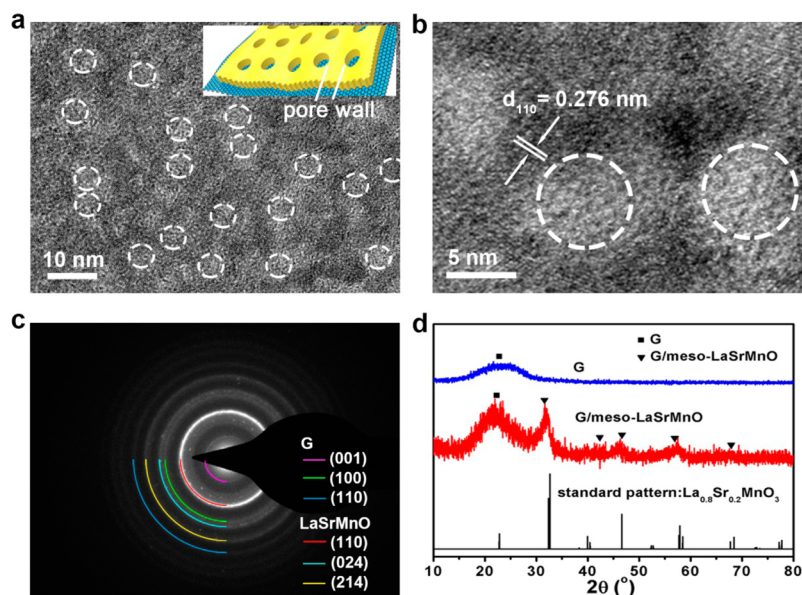
Figure 2. TEM images of the G/*meso*-LaSrMnO at (a) low and (b) high magnifications. Inset of (a) is the structural model of the G/*meso*-LaSrMnO. The crystal fringes of 0.276 nm are clearly seen, which is consistent with the *d* spacings of the (110) planes of LaSrMnO. The white dashed circles highlight mesopores existing in the *meso*-LaSrMnO layer and the pores are interconnected by crystalline domains. (c) SAED pattern of G/*meso*-LaSrMnO. The calculated *d* spacings from the SAED pattern are consistent with the *d*-spacing values for the corresponding planes of graphene and LaSrMnO. (d) XRD patterns of G, G/*meso*-LaSrMnO, and the standard pattern of $La_{0.8}Sr_{0.2}MnO_3$.

that the bulk G/*meso*-LaSrMnO foams are mechanically robust, which can be freely compressed and bended without structural damage (Scheme 1b). The overall excellent mechanical performance of the freestanding G/*meso*-LaSrMnO foam is attributed to the presence of a stable and robust graphene network.

RESULTS AND DISCUSSION

Scanning electron microscopy (SEM) images show that the G-foam maintains a highly porous 3D structure before and after coating of *meso*-LaSrMnO; the macropores enclosed by the graphene walls have sizes of several to tens of micrometers and form interconnected channels throughout the entire foam (Figure 1a,b). The graphene walls in the original G-foam are very thin and flexible and have a smooth surface with typical wrinkling (Figure 1c). It can be seen that the *meso*-LaSrMnO forms a very thin and conformal coating on the graphene walls (Figure 1d). The initially smooth graphene surface becomes rough and the interface between graphene and *meso*-LaSrMnO can be observed at regions where some LaSrMnO has detached from graphene. Both the top and bottom surface of graphene
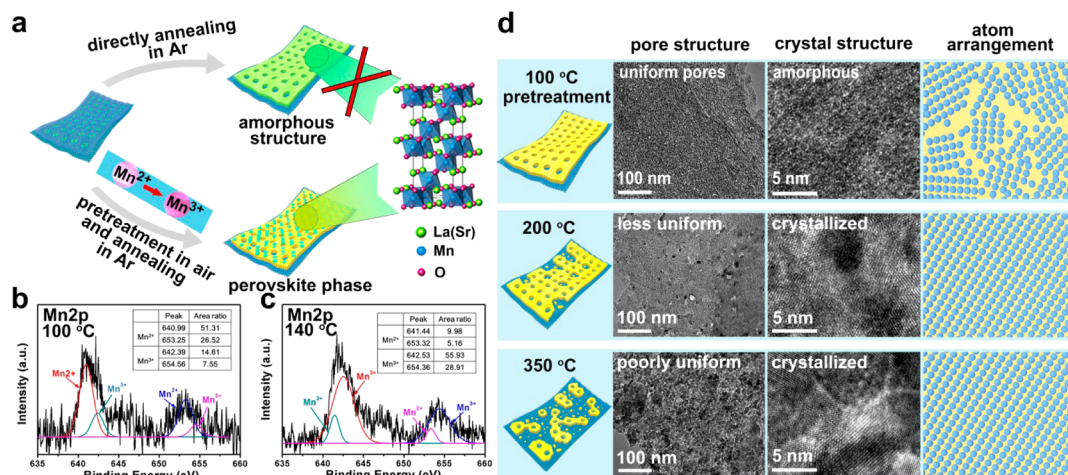
Figure 3. Investigation of the formation mechanism of *meso*-LaSrMnO. (a) Schematic illustration of the formation process of perovskite structure under different reaction conditions. A pretreatment in air for the valence state change of Mn element is essential for the final perovskite phase. High-resolution XPS spectra of the Mn 2p peak after preheat treatment at temperatures of (b) 100 and (c) 140 °C, respectively. Insets are the corresponding area ratio of Mn^{2+} and Mn^{3+}. (d) Structural model, TEM images, and crystal atom arrangement of G/*meso*-LaSrMnO nanosheets formed at preheat treatment temperatures of 100, 200, and 350 °C, respectively.

walls have been coated by the *meso*-LaSrMnO layer due to infiltration of precursor solution throughout the G-foam, resulting in a sandwich structure consisting of a graphene nanosheet in the middle and two mesoporous layers on two sides. Atomic force microscopy (AFM) characterization shows that the *meso*-LaSrMnO coating on graphene has a thickness of about 3 nm, with a rough surface morphology due to the uniform embedding of mesopores (Figure S2). The EISA method produced uniform deposition of *meso*-LaSrMnO among the porous G-foam, without producing undesired large particles or aggregates. Both the G-foam and G/*meso*-LaSrMnO foam show similar macroscopic morphology (Supporting Information, Figure S1).

The mesoporous structure of LaSrMnO coated graphene nanosheets were characterized by transmission electron microscopy (TEM). The LaSrMnO was deposited on the graphene nanosheets homogeneously as a continuous layer and embedded with uniformly distributed mesopores (Figure 2a). The presence of a large amount of mesopores can be distinguished from the white contrast areas (enclosed by dashed circles) among the LaSrMnO layer (Figure 2a). It is the EISA process that enables the formation of uniform mesopores rather than monodispersed nanoparticles. High-resolution TEM image clearly reveals the crystalline fringes interconnected by high-degree crystallized domains in the *meso*-LaSrMnO layer and the pore size is about 5 nm (Figure 2b). The selected-area electron diffraction (SAED) patterns taken from the G/*meso*-LaSrMnO nanosheets show distinct diffraction rings of graphene and *meso*-LaSrMnO at different crystal planes (Figure 2c), inconsistent with X-ray diffraction (XRD) patterns of the G/*meso*-LaSrMnO with well-crystallized perovskite-type oxides (JCPDS no. 53-0058) (Figure 2d). The original graphene nanosheets only displays two diffraction peaks corresponding to (002) and (100) crystal planes, in accordance with SAED patterns (Figure S3b). To further confirm the uniform distribution of *meso*-LaSrMnO on graphene, the dark field measurements and corresponding elemental mappings of C and La, Sr, Mn, and O were systemically conducted. The results demonstrate that each element is homogeneously dispersed on the graphene nanosheets (Figure S4). In addition, X-ray photoelectron spectroscopy (XPS) clearly

shows the appearance of La, Sr, and Mn peaks after *meso*-LaSrMnO deposition (Figure S5). The above results therefore demonstrate that the nanostructure of uniform mesoporous yet highly crystalline LaSrMnO coating on graphene was obtained with the proposed method.

It was found that the successful synthesis of uniform *meso*-LaSrMnO type oxides relied on the control over the preheat treatment temperature. As illustrated in Figure 3a, direct annealing under inert atmosphere always results in the formation of amorphous structure as the inert condition makes metal oxides difficult to crystallize.[31,34] In this proposed method, a suitable preheat temperature under air atmosphere induces the valence state transformation of Mn element and results in the perovskite crystal phase formation. This can be confirmed by the magnified XPS of the Mn 2p, in which the content of Mn^{3+} was enhanced significantly when the preheat temperature increased from 100 to 140 °C (Figure 3b,c). In addition, the preheat temperature also influences the distribution of mesopores and the crystalline degree of LaSrMnO (Figure 3d). At a lower temperature (100 °C), the resulting *meso*-LaSrMnO shows uniformly distributed mesopores but the window connecting the pores is amorphous according to the XRD pattern (Figure S6). When the temperature increases to 200 °C or even higher, a well-crystallized perovskite phase forms but there are decreased numbers of pores with less uniform distribution as indicated by the HRTEM images (Figure 3d). The formation of less uniform pores is due to the decomposition of the surfactant F127 at higher temperature, as indicated by the thermogravimetric analysis (TGA) curves (Figure S7). Once the surfactant decomposed partly under air, less uniform *meso*-LaSrMnO (200 °C) or large particles dispersed on the graphene nanosheets (350 °C) were obtained (Figure 3d and Figure S8). Therefore, in addition to fine control of the hydrolysis and condensation of precursors in a slow way, adjusting the preheat treatment temperature is also an important factor to obtain uniform, conformal, perovskite-phase *meso*-LaSrMnO coating on graphene.

N_2 adsorption—desorption curves of the original and mesoporous layer coated graphene foams both display type IV curves with distinct hysteresis loops of H4 type (Figure S9a). The

Brunauer–Emmett–Teller (BET) surface area has increased from 305 (G-foam) to 500 m^2·g^{-1} (G/*meso*-LaSrMnO) with a total pore volume of 0.74 cm^3·g^{-1}. Pore size distribution curves also show increased percentage of mesopores in the range of 2–50 nm after *meso*-LaSrMnO coating (Figure S9b). From TGA measurements, the original graphene foam starts to decompose at 300 °C derived from the instability of surface oxygen-containing groups, followed by a dramatic gravimetric loss from 550 to 640 °C upon combustion (Figure S10). After the *meso*-LaSrMnO coating, the loss of functional groups has disappeared but the combustion temperature decreases to 400–500 °C as the transition-metal oxide coating can decrease the decomposition temperature of graphene. TGA curves also indicate that the weight fraction (loading) of *meso*-LaSrMnO is about 30 wt % in the G/*meso*-LaSrMnO foam.

Porous metal oxides easily collapse under small deformation due to the inherent fragility of oxides framework, and the compressive stress–strain curve of a pure *meso*-LaSrMnO monolith shows quick collapse at small strain (Figure 4a). In
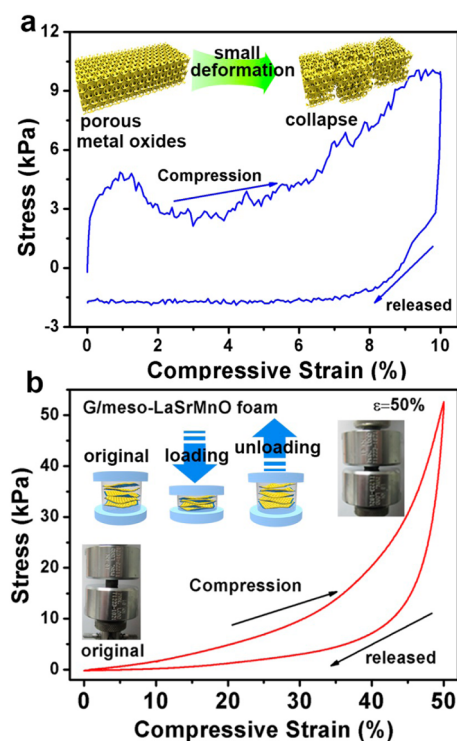

Figure 4. Mechanical performance of G/*meso*-LaSrMnO electrodes. Compressive stress–strain curves of (a) a *meso*-LaSrMnO monolith and (b) a G/*meso*-LaSrMnO foam at a specific strain of 50%, respectively. Inset shows the structural model of the *meso*-LaSrMnO monolith and G/*meso*-LaSrMnO foam at the original and compressed states.

contrast, the G/*meso*-LaSrMnO foam can be compressed to large strains of 50% without structural degradation and then recover to its original shape when the load is released (Figure 4b). This superior mechanical performance and elastic behavior stem from (1) the incorporation of a flexible 3D graphene scaffold to support *meso*-LaSrMnO and (2) the mechanical reinforcement of the *meso*-LaSrMnO coating to the G-foam. Furthermore, this composite foam may serve as porous and conductive bulk electrodes for energy devices. In particular, the macropores in the G/*meso*-LaSrMnO foam enables efficient O$_2$ and Li$^+$ diffusion

through the channels between the nanosheets, the mesopores in the LaSrMnO coating provide sufficient surface area for discharge products deposition, and graphene serves as a highly conductive substrate. Thus, the G/*meso*-LaSrMnO foam with optimized architecture can be directly used as freestanding flexible electrodes of Li–O$_2$ cells.

The catalytic performance of G and G/*meso*-LaSrMnO foam for the ORR and OER was evaluated by linear scanning voltammetry (LSV). From the rotating-disk-electrode (RDE) measurements, we observed much higher ORR current density (0.90 and 0.36 mA·cm^{-2} for G/*meso*-LaSrMnO and graphene, respectively) and onset potential (2.86 and 2.60 V for G/*meso*-LaSrMnO and graphene, respectively) in the G/*meso*-LaSrMnO foam than G-foam even at a low loading density of 0.125 mg·cm^{-2}, indicating significantly enhanced catalytic activity after coating *meso*-LaSrMnO (Figure 5). Also, the OER process of the composite electrode shows superior performance than the G-foam (Figure S11).
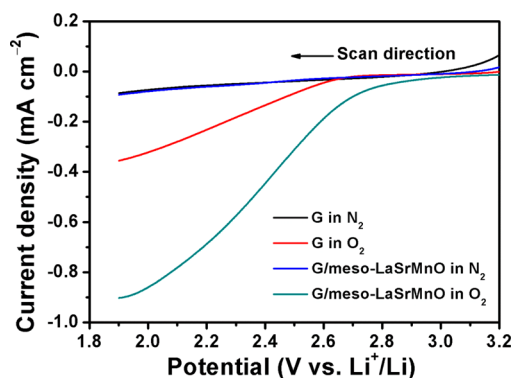
Figure 5. ORR measurements of the pure G and G/*meso*-LaSrMnO electrode under N$_2$ and O$_2$ atmosphere with a catalyst loading of 0.125 mg·cm^{-2}, a voltage sweep rate of 10 mV·s^{-1}, and a rotating speed of 900 rpm.

The G/*meso*-LaSrMnO foam as Li–O$_2$ cell cathode at various current densities was investigated with LiTFSI (lithium bis(trifluoromethanesulfonyl) imide) in TEGDME (tetraethylene glycol dimethyl ether) as electrolyte. It is worth mentioning that the G/*meso*-LaSrMnO foam was directly used as the Li–O$_2$ cell cathode without binder or conductive additive. From the charge/discharge curves, it can be seen that the G/*meso*-LaSrMnO electrode exhibits higher discharge potential and capacity performance at all investigated current densities (100–1000 mA·g^{-1}) (Figure 6a, Figure S12). The discharge voltage platform of the G/*meso*-LaSrMnO electrode is 2.77 V (*versus* Li$^+$/Li), significantly higher than the G-foam electrode (2.60 V). Apart from the high ORR activity, the G/*meso*-LaSrMnO electrode also exhibits much enhanced charging capability, as evidenced by the significantly decreased charging voltage plateau (3.80 vs 4.21 V for G-foam) during the charging process (Figure S12a). The charge/discharge performance is consistent with the RDE testing results, suggesting superior catalytic activity of the G/*meso*-LaSrMnO for both ORR and OER. It is obvious that the charge capacity is close to the discharge capacity at various current densities, demonstrating nearly 100% Coulombic efficiency and high charging efficiency of the G/*meso*-LaSrMnO electrode. The specific capacity reaches 6515 mAh·g^{-1} even at a high current density of 100 mA·g^{-1} when the total weight of the composite foam is calculated, corresponding to a capacity of 21470 mAh·g^{-1}
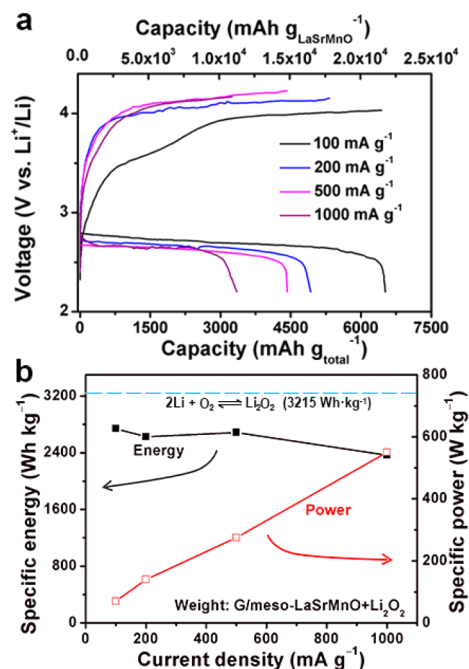
Figure 6. (a) Charge/discharge curves of Li−O$_2$ cells with G/*meso*-LaSrMnO electrode at different current densities of 100, 200, 500, 1000 mA·g^{-1}. (b) The specific energy and power of the Li−O$_2$ cell with G/*meso*-LaSrMnO electrode. The calculation is based on the total electrode and discharge product Li$_2$O$_2$.

with respect to catalyst loading and 9044 mAh·mL^{-1} with respect to the pore volume of the O$_2$ electrode. This is a 110% enhancement of the discharge performance compared to the cell with a pure graphene electrode (3120 mAh·g^{-1}). Furthermore, the hierarchical porous electrode displays excellent rate perform-ance, in which a discharge capacity of 3349 mAh·g^{-1} is still maintained even increasing the current density to 1000 mA·g^{-1} (10 times higher), corresponding to 51.4% capacity retention with respect to the original state, significantly higher than that of pure G electrode (14.9%) (Figure S12c). This is the best rate performance that has been reported on the basis of the perovskite electrode.[5,6,14] In addition, it did not show a drastic increase of polarization in the charge−discharge process as the applied current densities increased. The discharge capacity is 986 mAh·g^{-1} when the discharge product Li$_2$O$_2$ is included, corresponding to an energy density of 2741 Wh·kg$_{discharged}^{-1}$, which is 85% of the theoretical value (3215 Wh·kg$_{Li2O2}^{-1}$). As shown in Figure 6b, the specific energy *versus* power of the Li−O$_2$ cell with G/*meso*-LaSrMnO cathode. The calculations are normalized by the total weight of the electrode and the discharge product Li$_2$O$_2$. Surprisingly, the specific energy remains at a relative high value without degradation as the discharge rate increases. Even when the current density is increased to 1000 mA·g^{-1}, a specific energy of 2366 Wh·kg$_{discharged}^{-1}$ remains. This value is significantly higher than the theoretical value for a Li-ion battery, which is typically lower than 500 Wh·kg^{-1}. Substantial performance enhancement is believed to originate from the synergistic effect between the hierarchical flexible porous network of graphene and the *meso*-LaSrMnO catalyst layer. The interconnected macro-pores between nanosheets provide expanded transfer space and ensure easy oxygen access to the inner space of the electrode, the mesopores act as reservoirs of O$_2$ to feed the reaction, the inherent mechanical flexibility of G/*meso*-LaSrMnO enables its ability to withstand large volume change during charge/discharge

process, while the high surface area offers sufficient space for Li$_2$O$_2$ deposition and decomposition without clogging of the discharge products. Preheating the G/*meso*-LaSrMnO electrode at higher temperatures (200 and 350 °C) resulted in less uniform or poorly distributed mesopores and thus reduced specific capacity of 5959 and 5513 mAh·g^{-1} at 100 mA·g^{-1}, respectively (Figure S13). The capacity dropped to about 45.9% and 40% of the initial value when the current density was increased from 100 to 1000 mA·g^{-1}, indicating a lower rate performance than the electrode obtained under 140 °C pretreatment. SEM and TEM images after deep discharge show well maintained porous framework in the G/*meso*-LaSrMnO electrode (without blocking the Li$^+$ and O$_2$ transport channel) and recovery to the original state after recharge (complete decomposition of Li$_2$O$_2$) (Figure S14). Optical images of the G/*meso*-LaSrMnO electrode after the deep discharge and recharge state showed no obvious cracks existing on the electrode surface, indicating its mechanical flexibility and ability to withstand large volume change during the charge/discharge cycling (Figure S15).

The cyclic stability of the G/*meso*-LaSrMnO electrode was investigated at a relatively high current density of 500 mA·g^{-1} for 10 full cycles. The discharge capacity keeps at 2500−4500 mAh·g^{-1} even at the full charge/discharge state, with a high capacity retention of 55% (Figure 7a, b). In addition, there is no significant change of voltage difference in the charge curves during the cycling process (and also in the discharge curves). Our hierarchical porous and flexible electrode can accommodate the volume change arising from O$_2$/Li$_2$O$_2$ conversion between the charge/discharge process; such volume change may undermine the cycling stability of catalytic electrodes as reported before.[16] To further evaluate the cathode performance of the G/*meso*-LaSrMnO, we limited the capacity to 500 mAh·g^{-1} and recorded the charge/discharge behavior of the cells (Figure 7c, Figure S16). It is obvious that the catalytic performance is higher than the pure G electrode during the whole charge/discharge process. The pure G cathode can only be cycled at the limited capacity for 10 cycles due to the largely increased polarization. Addition of *meso*-LaSrMnO layer onto the G foam stabilize the electrode to 50 cycles and the Coulombic efficiency is nearly 100%. The enhanced performance is attributed to the reduction of the overpotential due to the high catalytic activity of perovskite based LaSrMnO, which can facilitate reversible conversion between O$_2$ and Li$_2$O$_2$. Since the electrolyte decomposition and volatilization are recognized issues, the reversibility of our Li−O$_2$ cell could be affected. In addition, the accumulated insoluble discharge products that remain on the electrode surface may block the catalyst sites and O$_2$ transfer channels and eventually leads to cell degradation (Figure S17). This implies that some degree of battery degradation is inevitable even if we limit the capacity to 500 mAh·g^{-1}. Nevertheless, in comparsion with perovskite and other material-based cathodes reported in the literature, our designed electrode has high specific capacity, power capability, and cycling stability (see details in the Supporting Information, Table S1). Furthermore, our electrode is freestanding and flexible and, thus, has the potential to serve as a flexible Li−O$_2$ cell electrode. Exposed carbon would react with electrolyte or reaction intermediates at charge potentials higher than 3.5 V, leading to capacity decrease and cell failure.[35,36] The conformal coating of the *meso*-LaSrMnO layer on graphene physically separates the carbon surface from Li$_2$O$_2$ and electrolyte and thus increases the carbon electrode stability. Raman spectra (Figure S18) and diffraction patterns (Figure S14e) indicate that the discharge product of the *meso*-LaSrMnO electrode is mainly
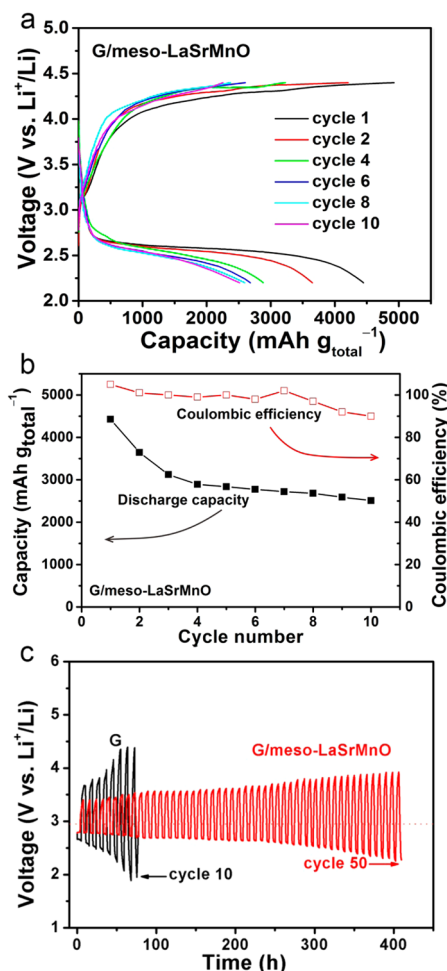
Figure 7. (a) Cyclic performance of the G/*meso*-LaSrMnO electrode at a specific current density of 500 mA·g^{-1} in full discharge. (b) Discharge capacity and Coulombic efficiency of the G/*meso*-LaSrMnO electrode at different cycles. (c) Voltage *versus* time graph of G and G/*meso*-LaSrMnO electrode at a discharge limit of 500 mAh·g^{-1}.

Li$_2$O$_2$ (a strong peak at 790 cm^{-1}), while another product Li$_2$CO$_3$ also appears in the pure G electrode due to the electrolyte and carbon species decomposition during the charge/discharge processes (Figure S19). The Li$_2$O$_2$ can be decomposed in the subsequent recharge process, while Li$_2$CO$_3$ remains at the electrode surface and impedes the charge/discharge process, resulting in lower cyclic stability. These results demonstrate that the well-designed hierarchical porous *meso*-LaSrMnO based electrodes have great potential as an ideal candidate for a Li−O$_2$ cell cathode.

CONCLUSION

In this work, we have synthesized mesoporous LaSrMnO in graphene foams by a facile soft chemistry method and constructed a 3D hierarchical architecture. Distinct from previously LaSrMnO-based nanostructures, we obtained a mesoporous yet crystalline LaSrMnO coating with uniform pore distribution on graphene by controlling key parameters. When employed as Li−O$_2$ cell electrodes, the G/*meso*-LaSrMnO foam shows significantly enhanced ORR and OER catalytic activity, high specific capacity, superior rate capability and cyclic stability. Combination of high catalytic activity mesoporous

perovskites with conductive graphene networks represents an effective strategy for developing efficient electrodes in various energy storage systems.

EXPERIMENTAL SECTION

Chemicals. Lanthanum nitrate hexahydrate (La(NO$_3$)$_3$·6H$_2$O, ≥98.0%), Strontiumnitrate (Sr(NO$_3$)$_2$, ≥99.5%), 50% manganese nitrate (Mn(NO$_3$)$_2$) water solution, sodium nitrate (NaNO$_3$, ≥99%), potassium hypermanganate (KMnO$_4$, ≥99.5%), citric acid monohydrate (C$_6$H$_8$O$_7$·H$_2$O, ≥99.5%), concentrated nitric acid (HNO$_3$, 65−68%), sulfuric acid (H$_2$SO$_4$, 95−98%), hydrogen peroxide (H$_2$O$_2$, ≥30%), and ethanol (≥99.7%) were provided by Beijing Fine Chemical Co. Graphite was purchased from Qingdao Jinrilai Co. High-purity argon gas (99.99%) was obtained from Haikeyuanchang of Beijing Gas Co.. Tretraethylene glycol dimethyl ether (TEGDME), lithium bis(trifluoromethanesulfonyl)imide (LiTFSI, ≥99.95%), and Pluronic F127 (M_w = 12600, PEO$_{106}$PPO$_{70}$PEO$_{106}$) were purchased from Sigma-Aldrich. The solvent TEGDME was further dried over freshly activated molecular sieves (type 4 Å) for 24 h.

Sample Characterization. TEM images were recorded on a FEI Tecnai G2 F20 (Tecnai F20) operated at 200 kV. The graphene and G/*meso*-LaSrMnO foams were separated in ethanol by sonication, and dispersed nanosheets were collected by copper grids for TEM characterization. SEM characterization was performed on a Hitachi S-4800 microscope (Hitachi, Japan). AFM was performed using Bruker Multimode8 operating in tapping mode. Raman spectra were recorded using an RM 2000 microscopic confocal Raman spectrometer (Renishaw PLC, England) with a 514 nm laser. TGA analysis was taken on a TGA Q5000 analyzer from 30 to 800 °C under air with a heating rate of 20 °C·min^{-1}. Nitrogen sorption isotherms were measured at 77 K using QUANTACHROME Autosorb-iQ analyzer. Before measurements, all of the samples were degassed in vacuum at 150 °C for 10 h. XPS measurements were performed using an ESCALAB 250Xi spectrometer. Mechanical measurements on graphene and G/*meso*-LaSrMnO foams were carried out by a single-column static instrument (Instron 5843) equipped with two flat compression stages and a 10 N load cell.

Electrochemical Measurements. Rotating disk electrode (RDE) measurements were carried out on a CHI 660D electrochemical workstation with a rotating disk electrode system (Pine Research Instrumentation, USA). A glass carbon disk electrode with 5 mm diameter was used as the working electrode, which was polished with 0.5 and 0.05 mm alumina paste prior to each experiment. The reference and counter electrodes were all metallic lithium pellets. As-prepared graphene or graphene/*meso*-LaSrMnO samples (1.25 mg) were dispersed in 500 μL of ethanol and ultrasonic dispersion to obtain a homogeneous ink. The film working electrode was prepared by drop-casting 10 μL catalyst ink on the Pt/C electrode, and then 10 μL of 5 wt % Nafion solution was dipped onto the electrode after catalyst dried, forming a catalyst loading of 0.0375 mg$_{catalyst}$·cm^{-2}. The thin film electrode was subsequently dried in air for 24 h before testing. The electrolyte, composed of 0.1 M LiTFSI in TEGDME solution, was prepared in the argon-filled glovebox. Nitrogen was introduced into the electrolyte for 30 min to ensure the data measured in inert atmosphere. Then pure oxygen was purged into the electrolyte for 10 min to study the electrocatalysis performance. Linear sweep voltammetry (LSV) studies were conducted at the potential of 1.9−3.3 V to study the ORR performance, and then a 2.25−4.5 V potential was applied to evaluate the OER performance.

Li−O$_2$ Cell Measurements. Li−O$_2$ cells were assembled in the Ar filled glovebox with oxygen and water contents less than 1 ppm. The cell structure consists of a stainless steel anode shell, a metallic lithium foil anode (0.5 mm thick), a glass fiber separator (from Whatman), a piece of as prepared oxygen cathode, a nickel foam current collector and a stainless steel cathode shell with holes in it, and 8 μL electrolyte composed of 1 M LiTFSI in TEGDME. The graphene or G/*meso*-LaSrMnO foam was directly used as cathode material without any conductive additive and binding agent. The galvanostatic discharge−charge performances of the Li−O$_2$ cells were measured by a Land

CT2001A battery system at various current densities within a voltage range from 2.2 to 4.4 V in a plastic box filled with high purity oxygen. The cycling performance was studied by fixing the capacity at 500 mAh·g^{-1} under a current density of 100 mA·g^{-1}. The gravimetric current density and specific capacity were calculated by the whole electrode material including graphene and *meso*-LaSrMnO.

Synthesis of Graphene Foam. Graphene oxide (GO) aqueous dispersions were prepared by a modified Hummers method. Typically, 0.5 g of graphite, 0.5 g of NaNO$_3$, and 23 mL of H$_2$SO$_4$ were stirred together in an ice bath. KMnO$_4$ (3 g) was added into the mixture slowly. Subsequently, the mixture was transferred into a 40 °C water bath and stirred for 1 h until a thick paste was formed. Next, 40 mL of water was added, and the solution was stirred for another 30 min while the temperature was raised to 90 °C. Finally, 100 mL of water and 3 mL of H$_2$O$_2$ were added in sequence, and the color of the solution turned from dark brown to yellow. The solution was centrifuged and washed with water until the pH of the solution reached 7. The final concentration of the resulting GO suspension was 3.9 mg·mL^{-1}, and the lateral size of the GO sheets ranging from 0.2 to 10 μm. For the synthesis of graphene foam, 600 μL of the GO solution was mixed with ascorbic acid (0.468 mg) in a 10 mL cylindrical glass vial, which was then placed in the oven and reacted at 75 °C for 12 h. The obtained gel was then immersed into the deionized water for 6 h to remove the soluble species, and then freeze-drying and thermal annealing at 200 °C in air for 2 h. Graphene foam with a density of 3.1 mg·cm^{-3} was obtained.

Fabrication of G/*meso*-LaSrMnO Foam. The G/*meso*-LaSrMnO foams were synthesized by a dip-coating strategy. Typically, 2 g of F127 was dissolved in a solvent mixture which was composed of 16 mL of ethanol and 4 mL of deionized water under magnetic stirring. 0.402 g of citric acid and 1 mL of HNO$_3$ was added into the above solution after the F127 dissolved. La(NO$_3$)$_3$·6H$_2$O (0.3248 g), Sr(NO$_3$)$_2$ (0.0529 g), and Mn(NO$_3$)$_2$ (116 μL) solution were added into the mixture and stirred for 12 h to obtain a homogeneous solution. A 2.5 mL portion of the above solution was added to a mixture of 6 mL of ethanol and 1.5 mL of H$_2$O to obtain the resulting precursor solution. The designed La/Sr/Mn ratio is 0.8/0.2/1. A piece of graphene foam was dipped into the mixture for a few minutes to adsorb the LaSrMnO precursor. The sample was placed in an oven with a temperature of 60 °C and undergoes an EISA process for 1 h, a subsequent 100 °C treatment for 1 h to remove the residue solvent, and 140 °C thermoreaction for 2 h. The resulting composite foams were placed in a furnace and calcined at a heating rate of 2 °C·min^{-1} to 400 °C for 2 h to remove surfactant F127 and then heated up to 650 °C for 2 h at a heating rate of 5 °C·min^{-1} to obtain the perovskite phase. The annealing was all performed in the argon atmosphere.

ASSOCIATED CONTENT

Ⓢ Supporting Information

The Supporting Information is available free of charge on the ACS Publications website at DOI: 10.1021/acsnano.5b06592.

> Optical, TEM, and SEM images of graphene and G/*meso*-LaSrMnO; SAED pattern of graphene; TEM-EDS mapping, XPS wide-scan spectra, XRD patterns, TGA curves, N$_2$ adsorption−desorption curves, pore size distributions, Raman spectra, RDE measurements, charge−discharge curves of Li−O$_2$ cell with graphene or G/*meso*-LaSrMnO electrode; SEM and TEM images of the electrode at different charge−discharge states (PDF)

AUTHOR INFORMATION

Corresponding Authors

*E-mail: anyuan@pku.edu.cn.
*E-mail: yuanquan@whu.edu.cn.

Notes

The authors declare no competing financial interest.

REFERENCES

(1) Si, W. Z.; Wang, Y.; Peng, Y.; Li, J. H. Selective Dissolution of A-Site Cations in ABO$_3$ Perovskites: A New Path to High-Performance Catalysts. *Angew. Chem., Int. Ed.* **2015**, *54*, 7954−7957.

(2) Sarshar, Z.; Kleitz, F.; Kaliaguine, S. Novel Oxygen Carriers for Chemical Looping Combustion: La$_{1-x}$Ce$_x$BO$_3$ (B = Co, Mn) Perovskites Synthesized by Reactive Grinding and Nanocasting. *Energy Environ. Sci.* **2011**, *4*, 4258−4269.

(3) Wang, X. Y.; Qi, X. X.; Chen, Z. L.; Jiang, L. L.; Wang, R. H.; Wei, K. M. Studies on SO$_2$ Tolerance and Regeneration over Perovskite-Type LaCo$_{1-x}$Pt$_x$O$_3$ in NO$_x$ Storage and Reduction. *J. Phys. Chem. C* **2014**, *118*, 13743−13751.

(4) Suntivich, J.; Gasteiger, H. A.; Yabuuchi, N.; Nakanishi, H.; Goodenough, J. B.; Shao-Horn, Y. Design Principles for Oxygen-reduction Activity on Perovskite Oxide Catalysts for Fuel Cells and Metal-air Batteries. *Nat. Chem.* **2011**, *3*, 546−550.

(5) Xu, J. J.; Xu, D.; Wang, Z. L.; Wang, H. G.; Zhang, L. L.; Zhang, X. B. Synthesis of Perovskite-Based Porous La$_{0.75}$Sr$_{0.25}$MnO$_3$ Nanotubes As a Highly Efficient Electrocatalyst for Rechargeable Lithium-Oxygen Batteries. *Angew. Chem., Int. Ed.* **2013**, *52*, 3887−3890.

(6) Jung, J.; Jeong, H. Y.; Kim, M. G.; Nam, G.; Park, J.; Cho, J. Fabrication of Ba$_{0.5}$Sr$_{0.5}$Co$_{0.8}$Fe$_{0.2}$O$_{3-\delta}$ Catalysts with Enhanced Electrochemical Performance by Removing an Inherent Heterogeneous Surface Film Layer. *Adv. Mater.* **2015**, *27*, 266−271.

(7) Zhao, Y. L.; Xu, L.; Mai, L. Q.; Han, C. H.; An, Q. Y.; Zhang, Q. J. Hierarchical Mesoporous Perovskite La$_{0.5}$Sr$_{0.5}$CoO$_{2.91}$ Nanowires with Ultrahigh Capacity for Li-air Batteries. *Proc. Natl. Acad. Sci. U. S. A.* **2012**, *109*, 19569−19574.

(8) Thotiyl, M. M. O.; Freunberger, S. A.; Peng, Z. Q.; Chen, Y. H.; Liu, Z.; Bruce, P. G. A Stable Cathode for the Aprotic Li-O$_2$ battery. *Nat. Mater.* **2013**, *12*, 1050−1056.

(9) Jung, H. G.; Hassoun, J.; Park, J. B.; Sun, Y. K.; Scrosati, B. An Improved High-performance Lithium-air Battery. *Nat. Chem.* **2012**, *4*, 579−585.

(10) Peng, Z.; Freunberger, S. A.; Chen, Y. H.; Bruce, P. G. A Reversible and Higher-Rate Li-O$_2$ Battery. *Science* **2012**, *337*, 563−566.

(11) Bruce, P. G.; Freunberger, S. A.; Hardwick, L. J.; Tarascon, J. M. Li−O$_2$ and Li−S Batteries with High Energy Storage. *Nat. Mater.* **2011**, *11*, 19−29.

(12) Grande, L.; Paillard, E.; Hassoun, J.; Park, J. B.; Lee, Y. J.; Sun, Y. K.; Passerini, S.; Scrosati, B. The Lithium/Air Battery: Still an Emerging System or a Practical Reality? *Adv. Mater.* **2015**, *27*, 784−800.

(13) Xie, J.; Yao, X. H.; Cheng, Q. M.; Madden, I. P.; Dornath, P.; Chang, C. C.; Fan, W.; Wang, D. W. Three Dimensionally Ordered Mesoporous Carbon As a Stable, High-Performance Li-O$_2$ Battery Cathode. *Angew. Chem., Int. Ed.* **2015**, *54*, 4299−4304.

(14) Guo, Z. Y.; Zhou, D. D.; Dong, X. L.; Qiu, Z. J.; Wang, Y. G.; Xia, Y. Y. Ordered Hierarchical Mesoporous/Macroporous Carbon: A High-Performance Catalyst for Rechargeable Li-O$_2$ Batteries. *Adv. Mater.* **2013**, *25*, 5668−5672.

(15) Lim, H. D.; Song, H.; Kim, J.; Gwon, H.; Bae, Y.; Park, K. Y.; Hong, J.; Baughman, R. H.; Kang, K. Superior Rechargeability and Efficiency of Lithium−Oxygen Batteries: Hierarchical Air Electrode Architecture Combined with a Soluble Catalyst. *Angew. Chem., Int. Ed.* **2014**, *53*, 3926−3931.

(16) Lim, H. D.; Park, K. Y.; Song, H.; Jang, E. Y.; Gwon, H.; Baughman, R. H.; Kang, K. Enhanced Power and Rechargeability of a Li−O$_2$ Battery Based on a Hierarchical-Fibril CNT Electrode. *Adv. Mater.* **2013**, *25*, 1348−1352.

(17) McCloskey, B. D.; Scheffler, R.; Speidel, A.; Bethune, D. S.; Shelby, R. M.; Luntz, A. C. On the Efficacy of Electrocatalysis in

Nonaqueous Li-O$_2$ Batteries. *J. Am. Chem. Soc.* **2011**, *133*, 18038−18041.

(18) Black, R.; Lee, J. H.; Adams, B.; Mims, C. A.; Nazar, L. F. The Role of Catalysts and Peroxide Oxidation in Lithium-Oxygen Batteries. *Angew. Chem., Int. Ed.* **2013**, *52*, 392−396.

(19) Grimaud, A.; May, K. J.; Carlton, C. E.; Lee, Y. L.; Risch, M.; Hong, W. T.; Zhou, J. G.; Shao-Horn, Y. Double Perovskites As A Family of Highly Active Catalysts for Oxygen Evolution in Alkaline Solution. *Nat. Commun.* **2013**, *4*, 2439−2445.

(20) Suntivich, J.; May, K. J.; Gasteiger, H. A.; Goodenough, J. B.; Shao-Horn, Y. A Perovskite Oxide Optimized for Oxygen Evolution Catalysis from Molecular Orbital Principles. *Science* **2011**, *334*, 1383−1385.

(21) Cui, Z. M.; Li, L. J.; Manthiram, A.; Goodenough, J. B. Enhanced Cycling Stability of Hybrid Li-Air Batteries Enabled by Ordered Pd$_3$Fe Intermetallic Electrocatalyst. *J. Am. Chem. Soc.* **2015**, *137*, 7278−7281.

(22) Lei, Y.; Lu, J.; Luo, X. Y.; Wu, T. P.; Du, P.; Zhang, X. Y.; Ren, Y.; Elam, J. W.; Amine, K. Synthesis of Porous Carbon Supported Palladium Nanoparticle Catalysts by Atomic Layer Deposition: Application for Rechargeable Lithium-O$_2$ Battery. *Nano Lett.* **2013**, *13*, 4182−4189.

(23) Li, F. J.; Tang, D. M.; Chen, Y.; Golberg, D.; Kitaura, H.; Zhang, T.; Yamada, A.; Zhou, H. S. Ru/ITO: A Carbon-Free Cathode for Nonaqueous Li-O$_2$ Battery. *Nano Lett.* **2013**, *13*, 4702−4707.

(24) Fu, Z. H.; Lin, X. J.; Huang, T.; Yu, A. S. Nano-sized La$_{0.8}$Sr$_{0.2}$MnO$_3$ As Oxygen Reduction Catalyst in Nonaqueous Li/O2 Batteries. *J. Solid State Electrochem.* **2012**, *16*, 1447−1452.

(25) Rostamnejadi, A.; Salamati, H.; Kameli, P.; Ahmadvand, H. Superparamagnetic Behavior of La$_{0.67}$Sr$_{0.33}$MnO$_3$ Nanoparticles Prepared *via* Sol-gel Method. *J. Magn. Magn. Mater.* **2009**, *321*, 3126−3131.

(26) Huang, K. K.; Chu, X. F.; Feng, W. C.; Zhou, C. P.; Si, W. Z.; Feng, S. H. Catalytic Behavior of Electrospinning Synthesized La$_{0.75}$Sr$_{0.25}$MnO$_3$ Nanofibers in the Oxidation of CO and CH$_4$. *Chem. Eng. J.* **2014**, *244*, 27−32.

(27) Zhu, Y. W.; Murali, S.; Cai, W. W.; Li, X. S.; Suk, J. W.; Potts, J. R.; Ruoff, R. S. Graphene and Graphene Oxide: Synthesis, Properties, and Applications. *Adv. Mater.* **2010**, *22*, 3906−3924.

(28) Qiu, L.; Liu, J. Z.; Chang, S. L. Y.; Wu, Y. Z.; Li, D. Biomimetic Superelastic Graphene-based Cellular Monoliths. *Nat. Commun.* **2012**, *3*, 1241−1247.

(29) Sun, H. Y.; Zhen, X.; Gao, C. Multifunctional, Ultra-Flyweight, Synergistically Assembled Carbon Aerogels. *Adv. Mater.* **2013**, *25*, 2554−2560.

(30) Li, Z.; Liu, Z.; Sun, H. Y.; Gao, C. Superstructured Assembly of Nanocarbons: Fullerenes, Nanotubes, and Graphene. *Chem. Rev.* **2015**, *115*, 7046−7117.

(31) Zhou, W.; Li, W.; Wang, J. Q.; Qu, Y.; Yang, Y.; Xie, Y.; Zhang, K. F.; Wang, L.; Fu, H. G.; Zhao, D. Y. Ordered Mesoporous Black TiO$_2$ As Highly Efficient Hydrogen Evolution Photocatalyst. *J. Am. Chem. Soc.* **2014**, *136*, 9280−9283.

(32) Li, W.; Yue, Q.; Deng, Y. H.; Zhao, D. Y. Ordered Mesoporous Materials Based on Interfacial Assembly and Engineering. *Adv. Mater.* **2013**, *25*, 5129−5152.

(33) Cote, L. J.; Kim, F.; Huang, J. X. Langmuir-Blodgett Assembly of Graphite Oxide Single Layers. *J. Am. Chem. Soc.* **2009**, *131*, 1043−1049.

(34) Lee, J.; Orilall, M. C.; Warren, S. C.; Kamperman, M.; Disalvo, F. J.; Wiesner, U. Direct Access to Thermally Stable and Highly Crystalline Mesoporous Transition-metal Oxides with Uniform Pores. *Nat. Mater.* **2008**, *7*, 222−228.

(35) Ottakam Thotiyl, M. M.; Freunberger, S. A.; Peng, Z. Q.; Bruce, P. G. The Carbon Electrode in Nonaqueous Li-O$_2$ Cells. *J. Am. Chem. Soc.* **2013**, *135*, 494−500.

(36) Itkis, D. M.; Semenenko, D. A.; Kataev, E. Y.; Belova, A. I.; Neudachina, V. S. Reactivity of Carbon in Lithium-Oxygen Battery Positive Electrodes. *Nano Lett.* **2013**, *13*, 4697−4701.